

Diverse Sampling for Normalizing Flow Based Trajectory Forecasting

Yecheng Jason Ma
University of Pennsylvania
jasonyma@seas.upenn.edu

Jeevana Priya Inala
MIT CSAIL
jinala@csail.mit.edu

Dinesh Jayaraman, Osbert Bastani
University of Pennsylvania
{dineshj, obastani}@seas.upenn.edu

Abstract

For autonomous cars to drive safely and effectively, they must anticipate the stochastic future trajectories of other agents in the scene, such as pedestrians and other cars. Forecasting such complex multi-modal distributions requires powerful probabilistic approaches. Normalizing flows have recently emerged as an attractive tool to model such distributions. However, when generating trajectory predictions from a flow model, a key drawback is that independent samples often do not adequately capture all the modes in the underlying distribution. We propose *Diversity Sampling for Flow (DSF)*, a method for improving the quality and the diversity of trajectory samples from a pre-trained flow model. Rather than producing individual samples, DSF produces a set of trajectories in one shot. Given a pre-trained forecasting flow model, we train DSF using gradients from the model, to optimize an objective function that rewards high likelihood for individual trajectories in the predicted set, together with high spatial separation between trajectories. DSF is easy to implement, and we show that it offers a simple plug-in improvement for several existing flow-based forecasting models, achieving state-of-art results on two challenging vehicle and pedestrian forecasting benchmarks.

1. Introduction

A key challenge facing self-driving cars is accurately forecasting the future trajectories of other vehicles. These future trajectories are often diverse and multi-modal, requiring a forecasting model to predict not a single ground truth future but the full range of plausible futures [29]. We focus on forecasting the trajectory of a single agent [6, 35], though our approach can easily be extended to multiple agents.

With the increasing abundance of driving data [5, 7], a promising approach is to learn a deep generative model from data to predict the probability distribution over future trajectories [28, 18, 24, 43, 38, 40]. We focus on normalizing flows [33], a powerful family of generative models that

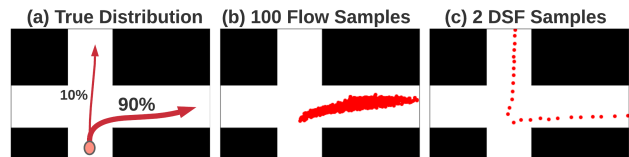


Figure 1: (a) At this intersection, 90% of cars turn right, and 10% drive straight in our training dataset. (b) A normalizing flow (NF) trajectory predictor trained on this data, sampled 100 times i.i.d., does not produce any straight trajectories. (c) With our DSF sampler plugged in, the same predictor generates both straight and right-turn trajectories with just 2 samples. Additional details are in Appendix B.

have recently been applied to this task [37, 38, 39, 1, 34]. A normalizing flow trajectory forecasting model defines an invertible mapping from a simple sampling distribution to the future trajectory distribution, given the observations. This allows not only easy sampling of future trajectories, but also exact likelihood computation for a candidate trajectory.

However, due to natural biases, sampling i.i.d. from a flow model’s prior distribution may fail to cover all modes in the trajectory distribution, especially given the uneven distribution of real-world traffic maneuvers. Consider the scenario in Figure 1(a). The i.i.d. forecasts from a flow model in Figure 1(b) successfully capture the major mode corresponding to turning right; however, for driving safely at this intersection, we must also anticipate the minor mode corresponding to vehicles driving straight.

We propose a general, *post-hoc* approach, called *Diversity Sampling for Flow (DSF)*, for enhancing the quality and the diversity of samples from a pre-trained flow model. The key idea is that rather than drawing i.i.d. samples from the flow model, DSF learns a sampling distribution over an entire *set* of trajectories, which jointly maximizes two objectives: (i) the likelihood of the trajectories according to the flow model, and (ii) a goal-based diversity objective that encourages high final spatial separation among trajectories. Intuitively, these two objectives together encourage a set of forecasts to cover modes in the un-

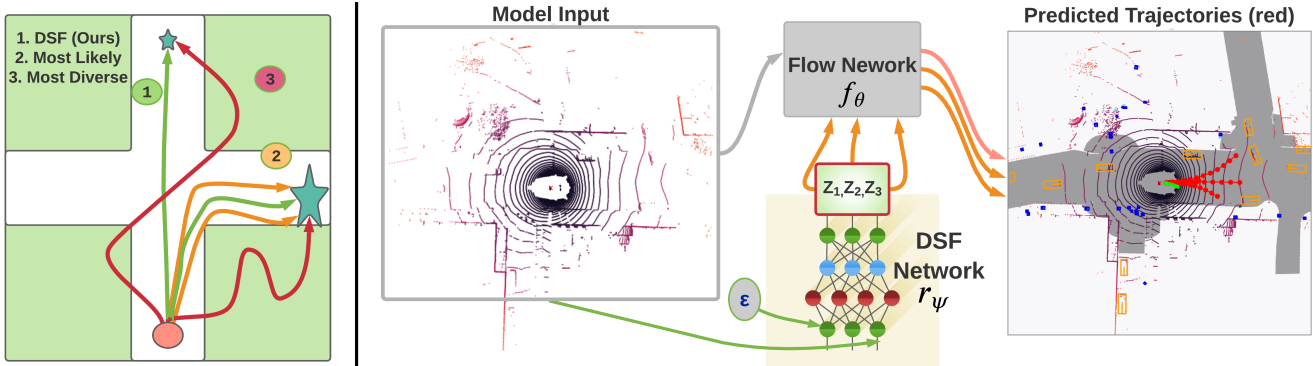


Figure 2: **Left:** Fitted on data at this intersection where most vehicles turn right and a small fraction head straight, **(1):** DSF predicts a set of paths that cover both modes and are realistic, **(2):** Optimizing for only model likelihood generates samples that are realistic but miss the minor mode (small star) at the top, and **3:** Optimizing for only diversity generates samples that may cover both modes but are not realistic. **Right:** DSF architecture overview. DSF replaces standard i.i.d. sampling in the flow model with a learned joint distribution over a set of samples in the latent space. These samples allow the pre-trained flow model to output diverse and realistic trajectories.

derlying trajectory distribution. The result of running DSF on our toy example is shown in Figure 1(c); it is able to discover the minor mode of traveling straight and distribute samples in both modes accordingly. Figure 2 provides an overview of the DSF objective and architecture.

The only assumption our approach requires is the ability to compute the exact likelihood of a given future trajectory. We focus on normalizing flow [36] based approaches, all of which possess this property. DSF is simple to implement, requiring fewer than 50 lines of code, and providing a reliable performance boost when plugged into various existing flow-based forecasting models. Note that DSF does not require additional labeled trajectory data for training, so it can also be used for *transductive learning* [44], directly improving predictions on a novel test instance without any prior training. This approach allows DSF to be tailored to produce good predictions in novel situations.

We evaluate DSF on both single-future and multi-future benchmarks. First, on the challenging nuScenes trajectory forecasting benchmark [5], we show that DSF significantly improves both the accuracy and diversity of samples from an autoregressive affine flow [39] forecasting model, enabling it to achieve state-of-art results. In addition, we also evaluate DSF on Forking Paths [29], a recently introduced multi-future pedestrian forecasting dataset, where each history trajectory is associated with multiple corresponding ground-truth futures. This dataset explicitly represents the underlying uncertainty in trajectory forecasting; in particular, diversity is necessary to achieve good performance. On this dataset, using DSF with an attention-based flow forecaster [34] significantly outperforms all prior methods.

2. Related Work

Multi-Modal Forecasting. A forecasting model operating in stochastic environments must be able to predict multiple possible futures. Recent approaches have tackled this problem by explicitly accounting for multi-modality in their model design choices. One approach is to pre-define trajectory primitives that serve as candidate outputs and formulate the forecasting problem as a mix of classification and regression [11, 6, 9, 35]. However, these approaches require extra labeled information; furthermore, they often only output a deterministic set of predictions for a given input.

Instead, we focus on more direct generative modeling-based approaches that explicitly output a multi-modal distribution [28, 43, 24, 40] and allow stochastic forecasting. These methods typically build on top of a deep generative model. In particular, normalizing flows [36, 33] have become a popular choice due to their comparative ease of optimization [37, 34, 39, 15], as well as their flexibility for downstream tasks such as goal-conditioned planning [38]. Our method is designed as a plug-in improvement for sampling better and more diverse predictions from any models pre-trained with this family of approaches.

Diversity Sampling. Prior work on obtaining diverse samples from deep generative models [20, 42, 31, 16, 19, 13, 23, 10] require architectural modifications, and cannot be applied to a pre-trained model. Improving the diversity of a pre-trained model has also been explored—for example, finding the M -best solutions in a Bayesian posterior [4], or using deterministic point processes [46, 17, 14]. In contrast, our approach models complex sampling distributions through a neural network-based sampler. The closest work to ours is DLow [47], a recent post-hoc sampling method

designed and demonstrated for conditional-VAEs (cVAEs) [41]. Similar to our method, DLow also jointly optimizes for the realism and the diversity of samples from the cVAE. Critically, DSF takes advantage of the ability of flow models to compute the exact likelihood of a trajectory. This enables gradient-based training to directly maximize the likelihood under the trajectory distribution rather than relying on stochastic samples from the distribution. It also permits transductive training without access to any labeled data. Across our experiments, DSF uniformly outperforms DLow by significant margins.

3. Problem Setup

Consider the problem of predicting the trajectory of an agent whose 2D position at time t is denoted as $\mathbf{S}_t = (x_t, y_t)$. We denote the current time step as $t = 0$, and the future aggregated state as $\mathbf{S} := \mathbf{S}_{1:T} \in \mathbb{R}^{T \times 2}$. At time $t = 0$, the agent has access to observation \mathbf{o} , which may include contextual features such as Lidar scans, physical attributes of the vehicle/pedestrian agent (e.g. velocity, yaw), and the state histories of all agents in the scene. The goal of trajectory forecasting is to predict \mathbf{S} given \mathbf{o} , $p(\mathbf{S}|\mathbf{o})$. We denote the training dataset as $\mathcal{D} = \{(\mathbf{o}, \mathbf{S})\}$.

Our approach assumes as given, a flow model f_θ that has been pre-trained to learn the distribution $p_\theta(\mathbf{S}|\mathbf{o}; \mathcal{D})$. At a high level, assuming a multivariate Gaussian base sampling distribution $\mathbf{Z} \sim P_{\mathbf{Z}} \equiv \mathcal{N}(0, \mathbf{I})$, f_θ is a bijective mapping between \mathbf{Z} and \mathbf{S} , captured by the following forward and inverse computations of f_θ :

$$\mathbf{S} = f_\theta(\mathbf{Z}; \mathbf{o}) \sim p_\theta(\mathbf{S} | \mathbf{o}), \quad \mathbf{Z} = f_\theta^{-1}(\mathbf{S}; \mathbf{o}) \sim P_{\mathbf{Z}} \quad (1)$$

To draw one trajectory sample \mathbf{S} , we sample $\mathbf{Z} \sim P_{\mathbf{Z}}$ and compute $\mathbf{S} = f_\theta(\mathbf{Z}; \mathbf{o})$. Furthermore, the exact likelihood of a trajectory \mathbf{S} is given by the change of variables rule:

$$\log p_\theta(\mathbf{S}|\mathbf{o}) = \log \left(p(\mathbf{Z}) \cdot \left| \det \frac{df_\theta}{d\mathbf{Z}} \Big|_{\mathbf{z}=f_\theta^{-1}(\mathbf{S}; \mathbf{o})} \right|^{-1} \right), \quad (2)$$

where the bijective property and standard architectural choices for f_θ permit easy computation of the determinant. We refer readers to Appendix A for a more detailed introduction to flow-based trajectory forecasting.

4. Diversity Sampling for Flow

In stochastic settings, it is often necessary to use $K > 1$ trajectory predictions rather than just one, to ensure that the samples cover the full range of possible stochastic futures; we assume the number of predictions K is a given hyperparameter. However, as Figure 1 shows, simply drawing K i.i.d. samples from the flow model f_θ may undersample from minor modes and fail to capture all potential outcomes. We propose an alternative strategy, which we call

Diversity Sampling for Flow (DSF), that learns a joint distribution over K samples $\{\mathbf{Z}_1, \dots, \mathbf{Z}_K\}$ in the latent space of f_θ . In doing so, it aims to improve the diversity of the trajectories $f_\theta(\mathbf{Z}_1), \dots, f_\theta(\mathbf{Z}_K)$ while maintaining their plausibility according to the flow model.

In particular, DSF trains a neural network r_ψ to transform a Gaussian distribution $\epsilon \sim \mathcal{N}(0, \mathbf{I})$ into a distribution over a set $\mathcal{Z} := \{\mathbf{Z}_1, \dots, \mathbf{Z}_K\} = r_\psi(\epsilon; \mathbf{o})$ of latent vectors given an observation \mathbf{o} . This set in turn induces a distribution over trajectories $\mathcal{S} := \{\mathbf{S}_1, \dots, \mathbf{S}_K\}$, where $\mathbf{S}_k = f_\theta(\mathbf{Z}_k; \mathbf{o})$ for each k . Since the distribution is defined over multisets of samples, the individual samples \mathbf{S}_k are no longer independent. Informally, they should be anti-correlated to ensure they cover different modes. We train r_ψ to minimize the following loss function:

$$L_{\text{DSF}}(\psi) := \text{NLL}(\psi) - \lambda_d L_d(\psi), \quad (3)$$

which combines the negative log likelihood (NLL) loss from the flow model and a goal diversity loss L_d . Figure 2 (Left) provides intuition for these two terms, and we explain them in detail below.

Likelihood Objective. The NLL term is defined as:

$$\text{NLL}(\psi) := -\log p_\theta(\{f_\theta(r_\psi(\epsilon; \mathbf{o}))\}) = -\sum_{k=1}^K \log p_\theta(\mathbf{S}_k | \mathbf{o}), \quad (4)$$

where $\log p_\theta(\mathbf{S}_k | \mathbf{o})$ is computed as in Equation (2). The NLL loss incentivizes DSF to output a set of forecasts which all have high likelihood according to the flow model f_θ . Since f_θ is trained to maximize the likelihood of the training trajectories \mathcal{D} , this selects trajectories that are plausible and likely to occur. However, this set of forecasts need not be diverse and may easily concentrate around the major mode in the underlying trajectory distribution if trained without additional supervision, as in the ‘‘most likely’’ trajectories in Figure 2 (Left).

Diversity Objective. To combat this tendency, the diversity term L_d in Equation (3) incentivizes *diverse* trajectory samples that reach different parts of the state space. Specifically, we measure diversity as the *minimum* pairwise squared L_2 distance between trajectory predictions at the last time step:

$$L_d(\psi) := \min_{i \neq j \in K} \|f_\theta(\mathbf{Z}_i)_T - f_\theta(\mathbf{Z}_j)_T\|^2. \quad (5)$$

The minimum formulation strongly incentivizes DSF to distribute its samples among different modes in the distribution, since any two predictions that are close to each other would significantly decrease L_d . While many other notions of distances between trajectories are compatible with our framework, we measure the distances at the last time step

Algorithm 1 Batch DSF Training

- 1: **Input:** Flow f_θ , Observation Batch $\{\mathbf{o}\}$
 - 2: Initialize DSF model r_ψ
 - 3: **for** $\mathbf{o}_i \in \{\mathbf{o}\}$ **do**
 - 4: Sample $\epsilon \sim \mathcal{N}(0, \mathbf{I})$
 - 5: Compute $\mathbf{Z}_1, \dots, \mathbf{Z}_K = r_\psi(\epsilon; \mathbf{o}_i)$
 - 6: Generate predictions $f_\theta(\mathbf{Z}_1), \dots, f_\theta(\mathbf{Z}_K)$
 - 7: Compute losses using Equations 4 & 5
 - 8: **end for**
 - 9: Perform stochastic gradient descent on ψ to minimize L_{DSF} (Equation 3)
 - 10: **Output:** Trained DSF model r_ψ
-

alone, since spatial separation between trajectory endpoints is a good measure of trajectory diversity in our applications. Finally, to train r_ψ , DSF minimizes L_{DSF} using stochastic gradient descent; it is summarized in Algorithm 1.

Transductive Learning. Note that the DSF loss function does not depend on access to any ground truth future trajectories, and relies only on the pre-trained flow model and unlabeled inputs \mathbf{o} . In this sense, DSF is an unsupervised algorithm. It can therefore be used *transductively*—i.e., it can adapt on the fly to a given new observation \mathbf{o} through “test-time training” [44, 25]. Given an unlabeled input \mathbf{o} , we can train a DSF model r_ψ tailored to \mathbf{o} . This algorithm, which we call **DSF-TD**, is summarized in Algorithm 2 in Appendix C. Compared to vanilla “batch” DSF, DSF-TD does not need to be trained offline with a large dataset, making it suitable for settings where little or no training data is available—e.g., the training set for the pre-trained flow model is unavailable. In addition, in some of our experiments, we find DSF-TD outperforms DSF since it tailors its predictions to the test data.

Implementation Details. DSF r_ψ is implemented as a 3-layer feed-forward neural network with K heads, each of which corresponds to the latent z_k for a single output in the predicted set. We assume access to the input embedding layers of the pre-trained flow model, which embeds high-dimensional (visual) input \mathbf{o} into lower dimensional feature vectors. These feature vectors are taken as input to DSF. Additionally, we fix the dimensions of the input Gaussian noise ϵ to be the same as the trajectory output \mathbf{S} from f_θ (i.e. $T \times 2$). Furthermore, to prevent the diversity loss from diverging, we clip it to a positive value. Additional details are in Appendix E.5 & F.3.

5. Experiments

Our experiments aim to address the following questions: **(1)** Does DSF boost performance across different pre-trained flow models? **(2)** How does DSF compare against

state-of-the-art approaches for vehicle and pedestrian trajectory prediction?, **(3)** How does transductive training for DSF (TD-DSF) compare against batch training? **(4)** Which components of DSF are most important for performance?

We address questions 1-3 via experiments on two qualitatively different datasets, nuScenes [5] and Forking Paths [29] (Section 5.3 and 5.4). For each one, we use a distinct pre-trained flow model with architecture and input representation tailored to that dataset. We address question 4 via an ablation study in Section 5.5.

5.1. Datasets and Models

We begin by describing our datasets, models, and evaluation metrics; see Appendix E & F for details on our model architectures and training algorithms. We will release code for replicating all our experiments if accepted.

5.1.1 NuScenes

We evaluate DSF on the nuScenes autonomous driving dataset [5]. Following prior work [9, 35, 15], the predictor takes as input the current observation (e.g., Lidar scan) and attributes (e.g., velocity) of a vehicle, and forecasts this vehicle’s trajectory over the next 6 seconds (i.e., 12 frames).

Models. We train an autoregressive affine flow model (**AF**) that takes visual inputs as our underlying flow model [39] for trajectory prediction. On top of **AF**, we train two variants of DSF. The first is **DSF-AF**, the batch version in Algorithm 1. The second is **DSF-AF-TD**, the transductive version in Algorithm 2, which we train using small unlabeled minibatches from the test set.

Baselines. Our first baseline is **DLow-AF**, which replaces DSF with DLow [47] on top of the AF. Next, since DLow was originally designed for use with conditional VAEs (cVAEs), we include DLow-CVAE, where we pre-train a cVAE [41] and train a corresponding DLow model. Our third baseline is **MTP-Lidar**, which is based on **Multi-modal Trajectory Predictions (MTP)** [9] as implemented in the nuScenes codebase, but modified to use Lidar observations to ensure fair comparison with our models.¹ We also include existing results for state-of-the-art models as reported in [35] (rows with * in Table 1).

5.1.2 Forking Paths

One limitation of most trajectory forecasting datasets such as nuScenes is that there is only a single ground-truth future trajectory for each training sample. To evaluate each forecasting model’s ability to predict diverse, plausible future trajectories, it is critical to evaluate the model against multiple ground-truth trajectories in a multi-future dataset. This

¹We find that Lidar observations consistently outperform the rasterized HD map observations used in the original dataset.

approach directly evaluates whether a model captures the intrinsic stochasticity in future trajectories. Therefore, we additionally evaluate DSF on the recent Forking Paths (FP) dataset [29]. FP recreates scenes from real-world pedestrian trajectory datasets [32, 3] in the CARLA simulator [12], and asks multiple human annotators to annotate future trajectories in the simulator, thereby creating multiple ground truth future pedestrian trajectories for each scene. The flow model takes as input the trajectory of a pedestrian over the past 3 seconds (i.e., 12 frames), and its goal is to predict their trajectory over the next 5 seconds (i.e., 20 frames).

Models. For this dataset, we use the recently introduced Cross-Agent Attention Model Normalizing Flow (**CAM-NF**) [34] as our underlying flow model for trajectory prediction. Compared to the perception-based flow model we use in nuScenes, CAM-NF only uses the historical trajectory of the agent and other surrounding agents in the scene, consistent with various prior methods [18, 2] in pedestrian forecasting; we leave exploring the utility of added perception modules as in [30, 29] to future work. Hence, $\mathbf{o} = \{\mathbf{S}_{-T_{\text{hist}}:0}^a\}_{a=1}^A$, where A is the number of pedestrians in the scene and T_{hist} the length of history. CAM-NF first encodes the history of all pedestrians in the scene using a LSTM encoder. Then, it computes cross-pedestrian attention feature vectors using self-attention [45] to model the influences of nearby pedestrians, and uses these attention vectors as features for a normalizing flow decoder, which outputs future trajectories of the predicted pedestrian; see Appendix F for details. As before, we train both **DSF** and **DSF-TD** on top of CAM-NF (see below for details).

Baselines. We compare to **DLow** applied to CAM-NF. All other baseline results are taken directly from [29] (rows with * in Table 3), including **Social-LSTM** [2], **Social-GAN** [18], **Next** [30], and **Multiverse** [29], as well as simple **Linear** and **LSTM** networks.

Training and Evaluation. We follow the procedure in [29]. We first train CAM-NF using VIRAT/ActEV [32, 3], the real-world datasets from which FP extracts simulated pedestrian scenes. Then, we train DSF on top of the pre-trained CAM-NF model using the training dataset (VIRAT/ActEV). Finally, we evaluate all models on FP using $K = 20$ samples against the multiple ground-truth futures. Since DSF-TD uses transductive learning, we directly train and evaluate r_ψ on FP using small minibatches as described in Algorithm 2.

An important challenge is that trajectories in FP have different (typically longer) lengths compared to trajectories in VIRAT/ActEV, since the human annotators provided trajectories of varying durations; this issue makes the forecasting problem on the test set more difficult.

5.2. Evaluation Metrics

We report minimum average displacement error **minADE_K** and final displacement error **minFDE_K** of K prediction samples $\hat{\mathbf{S}}_k$ compared to the ground truth trajectories $\mathbf{S}_1, \dots, \mathbf{S}_J$ [43, 6, 29]:

$$\begin{aligned} \text{minADE}_K(\hat{\mathbf{S}}, \mathbf{S}) &= \frac{\sum_{j=1}^J \min_{i \in K} \sum_{t=1}^T \|\hat{\mathbf{S}}_{i,t} - \mathbf{S}_t\|^2}{T \times J}, \\ \text{minFDE}_K(\hat{\mathbf{S}}, \mathbf{S}) &= \frac{\sum_{j=1}^J \min_{i \in K} \|\hat{\mathbf{S}}_{i,T} - \mathbf{S}_T\|^2}{J} \end{aligned}$$

These metrics are widely used in stochastic prediction tasks [43, 18] and tend to reward predicted sets of trajectories that are both diverse and realistic. In multi-future datasets ($J > 1$) such as Forking Paths, these metrics are standalone sufficient to evaluate both the diversity and the plausibility of model predictions, because a set of predictions that does not adequately cover all futures will naturally incur high errors. In single-future datasets ($J = 1$) such as nuScenes, however, they do not explicitly penalize a predicted set of trajectories that simply repeats trajectories close to the single ground truth one. To explicitly measure prediction diversity on nuScenes, we also report the minimum average self-distance **minASD_K** and minimum final self-distance **minFSD_K** between pairs of predictions samples:

$$\begin{aligned} \text{minASD}_K(\hat{\mathbf{S}}) &= \min_{i \neq j \in K} \frac{1}{T} \sum_{t=1}^T \|\hat{\mathbf{S}}_{i,t} - \hat{\mathbf{S}}_{j,t}\|^2 \\ \text{minFSD}_K(\hat{\mathbf{S}}) &= \min_{i \neq j \in K} \|\hat{\mathbf{S}}_{i,T} - \hat{\mathbf{S}}_{j,T}\|^2. \end{aligned}$$

These metrics evaluate the lower bound diversity among a predicted set of trajectories, and they tend to decrease as K increases since the predictions become more “crowded” around the modes already covered. Note that minFSD is identical to the diversity term in the DSF objective (Equation (5)). Several prior works have reported the *average* ASD (meanASD) and FSD (meanFSD) instead [46, 47]; however, we observe that minASD is a superior metric since it is more robust to outliers among the predictions (see Appendix E.8 for an illustrative example). For completeness, we also report meanASD and meanFSD in Appendix E.7; our findings are consistent with those presented here. Finally, since minFDE_K, minASD_K, and minFSD_K were not reported in previous work, we only report them for the models we implement.

All implemented models, except CVAE and flow models, take the number K of modes/number of samples in the prediction set as a hyperparameter. We report results for each metric using the corresponding model configurations—e.g., when measuring minASD₅, we use $K = 5$ for all models.

Method	Modes	minADE ₁ (↓)	minADE ₅ (↓)	minADE ₁₀ (↓)	minFDE ₅ (↓)	minFDE ₁₀ (↓)
MultiPath* [6]	64	5.05	2.32	1.96	–	–
MTP* [9]	16	4.55	3.32	3.25	–	–
CoverNet* [35]	232	4.73	2.14	1.72	–	–
MTP-Lidar	5, 10	4.68 ± 1.04	2.61 ± 0.17	1.84 ± 0.04	5.80 ± 0.49	3.72 ± 0.07
CVAE	N/A	4.20 ± 0.03	2.71 ± 0.03	2.08 ± 0.02	6.20 ± 0.05	4.58 ± 0.05
DLow-CVAE [47]	5, 10	–	2.23 ± 0.13	1.75 ± 0.03	5.00 ± 0.29	3.71 ± 0.08
AF	N/A	4.01 ± 0.05	2.86 ± 0.01	2.19 ± 0.03	6.26 ± 0.05	4.49 ± 0.07
DLow-AF	5, 10	–	2.11 ± 0.01	1.78 ± 0.05	4.70 ± 0.03	3.77 ± 0.13
DSF-AF (Ours)	5, 10	–	2.06 ± 0.09	1.66 ± 0.02	4.67 ± 0.25	3.58 ± 0.05
DSF-AF-TD (Ours)	5, 10	–	2.06 ± 0.03	1.65 ± 0.02	4.62 ± 0.07	3.50 ± 0.05

Table 1: NuScenes prediction error results (lower is better), including previously reported results (top), and results of DSF variants and newly implemented baselines (bottom). DSF-based models produce the most accurate predictions throughout.

5.3. Quantitative Results

NuScenes. In Table 1, we compare the prediction accuracy of DSF, DSF-TD, and the baselines described above. DSF and DSF-TD achieve the best overall performance.

Comparing AF to MTP-Lidar, we see that although AF achieves better one-sample prediction performance (i.e., minADE₁), it performs significantly worse than MTP-Lidar when more predictions are made. This confirms our hypothesis that i.i.d. samples from a flow model do not adequately capture diverse modes, causing it to fail to cover the ground truth with good accuracy. However, when AF is augmented with DSF, it outputs the most accurate sets of predictions.

Similarly, AF performs worse than CVAE, but DSF-AF outperforms DLow-CVAE in every metric. Interestingly, DLow-AF also slightly outperforms DLow-CVAE, reversing the relative ranking of CVAE and AF. This result suggests that flow models can be more powerful than CVAEs, but require post-hoc tuning to realize their potential. Next, DSF-AF outperforms DLow-AF, especially at $K = 10$ samples, showing the advantage of exploiting the exact likelihood provided by the flow model. Finally, DSF-AF-TD outperforms DSF-AF on all metrics, suggesting that transductively training DSF produces better predictions through on-the-fly specialization.

Next, we compare the models in terms of their prediction diversity in Table 2. DSF models consistently outperform the baseline models by a large margin. In particular, they are the only models whose diversity does not collapse when the number of modes increases from 5 to 10. This shows that DSF is more “efficient” with its samples, since it does not repeat any trajectories. In contrast, all other methods produce pairs of very similar predictions when $K = 10$. Given that DSF also produces accurate predictions, these results provide strong evidence that DSF is able to simultaneously optimize accuracy and diversity. Furthermore, DSF

Method	$K = 5$		$K = 10$	
	minASD ₅ (↑)	minFSD ₅ (↑)	minASD ₁₀ (↑)	minFSD ₁₀ (↑)
MTP-Lidar	1.74 ± 0.32	4.31 ± 1.60	0.97 ± 0.15	2.43 ± 0.34
CVAE	1.28 ± 0.03	2.99 ± 0.07	0.57 ± 0.02	1.30 ± 0.04
DLow-CVAE	2.64 ± 0.25	6.38 ± 0.65	1.18 ± 0.16	2.73 ± 0.43
AF	1.58 ± 0.02	3.75 ± 0.04	0.70 ± 0.01	1.63 ± 0.02
DLow-AF	2.56 ± 0.12	6.45 ± 0.24	1.05 ± 0.11	2.55 ± 0.28
DSF-AF (Ours)	3.13 ± 0.18	8.19 ± 0.26	2.11 ± 0.05	6.22 ± 0.09
DSF-AF-TD (Ours)	3.09 ± 0.07	8.15 ± 0.17	1.98 ± 0.03	5.91 ± 0.04

Table 2: NuScenes prediction diversity results. DSF models produce much more diverse predictions than other methods.

also achieves the highest diversity under the mean diversity metrics in Appendix E.7.

Forking Paths. We show results in Table 3. Note that the FP dataset comes with two different categories “45-Degree” and “Top Down” depending on the camera angle view of the human annotators; we report results for each category separately as in the original work.

We first discuss the left sub-table, which shows results on the ActEV/VIRAT test set. CAM-NF works well on this dataset, only outperformed by the current state-of-art method Multiverse [29]. Next, when we evaluate these models on the FP dataset, CAM-NF already outperforms all prior methods on all metrics. There are two takeaways from this result. First, normalizing flow models prove to be very strong baselines for trajectory forecasting, thus warranting special attention as in this work. Second, effective models for single-future prediction might not necessarily be as effective for multi-future predictions; the latter task requires the model to produce predictions that cover multiple plausible futures. With DSF, CAM-NF improves even further, outperforming all prior methods by a large margin. DSF-TD improves performance still further on FDE metrics, while performing on-par with DSF on ADE metrics.

Importantly, DSF significantly outperforms DLow trained with the same flow model CAM-NF, by larger margins than on nuScenes. We believe this is because the

Method	minADE ₁ (↓)		minADE ₂₀ (↓)		minFDE ₂₀ (↓)	
	minADE ₁ (↓)	minFDE ₁ (↓)	45-Degree	Top Down	45-Degree	Top Down
Linear*	32.19	60.92	213.2	197.6	403.2	372.9
LSTM*	23.98	44.97	201.0 ± 2.2	183.7 ± 2.1	381.5 ± 3.2	355.0 ± 3.6
Social-LSTM*	23.10	44.27	197.5 ± 2.5	180.4 ± 1.0	377.0 ± 3.6	350.3 ± 2.3
Social-GAN*	23.10	44.27	187.1 ± 4.7	172.7 ± 3.9	342.1 ± 10.2	326.7 ± 7.7
Next*	19.78	42.43	186.6 ± 2.7	166.9 ± 2.2	360.0 ± 7.2	326.6 ± 5.0
Multiverse*	18.51	35.84	168.9 ± 2.1	157.7 ± 2.5	333.8 ± 3.7	316.5 ± 3.4
CAM-NF	19.69 ± 0.15	39.12 ± 0.31	155.2 ± 2.4	140.8 ± 2.2	305.0 ± 4.6	282.2 ± 4.9
			144.5 ± 3.8	131.0 ± 8.06	284.6 ± 8.4	262.1 ± 20.46
			103.8 ± 6.9	93.4 ± 4.8	190.6 ± 16.3	173.4 ± 12.8
			105.1 ± 4.3	94.9 ± 2.1	188.7 ± 10.4	167.4 ± 4.8

Table 3: **Left:** CAM-NF and baselines’ results on ActEV/VIRAT. **Right:** Evaluation results on Forking Paths. DSF-augmented CAM-NF significantly outperforms all other methods, including Multiverse and DLow-augmented CAM-NF.

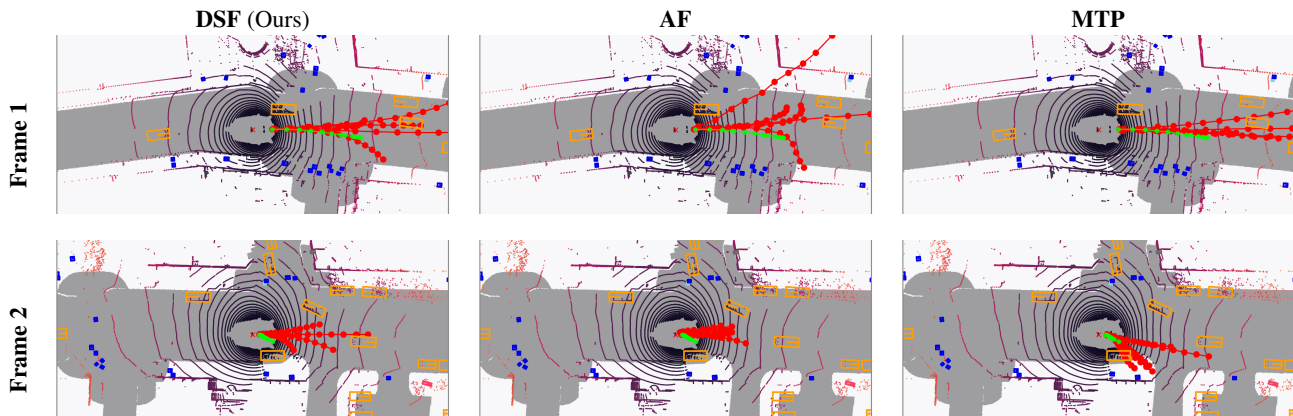


Figure 3: Model trajectory forecasts at two separate frames in the same scene. $K = 5$ predicted trajectories are shown in red, and the true recorded future trajectory from the dataset is shown in green. **DSF** predicts more diverse and plausible trajectories than both baselines.

ground truth futures in the FP test set tend to be longer than in the ActEV/VIRAT training set. Since DLow optimizes for the L_2 reconstruction loss between its forecasts and the ground-truth future trajectories in the *training* set, it is limited to improving diversity over the horizon of these training trajectories. Thus, it is unable to produce diverse predictions for longer horizon trajectories, such as those in the test set. In contrast, since DSF directly optimizes the likelihood of future trajectory according to the flow model, it does not rely on ground truth futures. Thus, it can improve diversity over much longer time horizons than in the training data. This contrast highlights the flexibility of DSF.

5.4. Qualitative Results

Here, we illustrate trajectories from DSF and baselines in the two benchmarks to demonstrate that DSF indeed outputs more diverse and plausible trajectories.

NuScenes. In Figure 3, we show visualizations of two separate frames of the same nuScenes instance, overlaid with

predictions from DSF, AF, and MTP-Lidar. Overall, DSF produces the most diverse and plausible set of trajectories in both frames. In the first frame, AF exhibits a failure mode as some of its predictions go far off the road. This provides evidence that sampling i.i.d. from a vanilla flow model may fail to identify realistic trajectories. But when DSF is used to draw samples from the same flow model (i.e., DSF-AF), the trajectories become both more diverse and more realistic. In the second frame, MTP-Lidar outputs a few trajectories that violate road constraints, while AF trajectories are concentrated in one cluster. Again, DSF-AF is the only model that predicts both diverse and plausible trajectories. We include additional visualizations in Appendix E.9.

Forking Paths. Visualizations of DSF (on top of CAM-NF), CAM-NF, and Multiverse predictions on the FP test set are shown in Figure 4. Additional visualizations are provided in Appendix F. DSF clearly outperforms the other two methods and is the only approach that comes close to covering the diverse ground-truth futures.

Method	$K = 5$				$K = 10$			
	mADE ₅ (↓)	mFDE ₅ (↓)	minASD ₅ (↑)	minFSD ₅ (↑)	mADE ₁₀ (↓)	mFDE ₁₀ (↓)	minASD ₁₀ (↑)	minFSD ₁₀ (↑)
Ours	2.06	4.62	3.09	8.15	1.65	3.50	1.98	5.91
Ours w.o. Diversity	5.95	14.63	0.16	0.37	4.97	12.52	0.07	0.15
Ours w.o. Likelihood	8.06	19.40	10.16	24.83	5.61	13.20	4.55	11.02
Ours w. Rec	2.16	4.89	3.29	9.00	1.78	3.85	2.92	5.73
Ours w. meanDiv	4.85	11.43	0.17	0.36	4.92	11.66	0.03	0.05

Table 4: DSF ablation results. In row 2-3, one of the DSF losses is removed, and performance significantly deteriorates. In row 4-5, one of the DSF losses is replaced by an alternative, and performance again declines sharply.

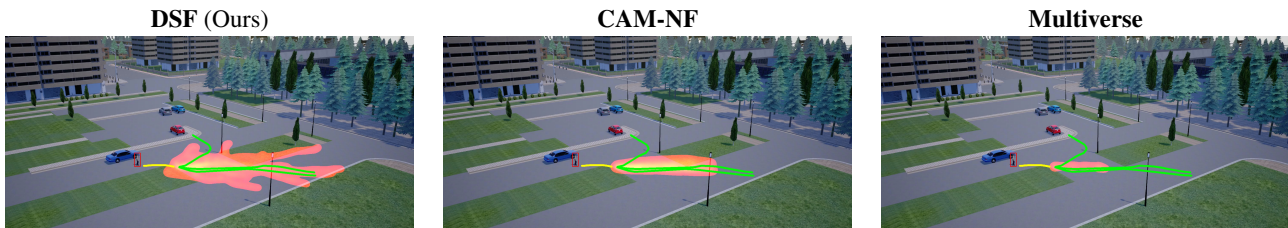


Figure 4: Visualization of predictions from various models on a single scene from the Forking Paths dataset. The red-yellow heatmap corresponds to the visited state density from the 20 predicted trajectories from each model; yellow indicates higher density. The green lines are the ground-truth human annotated futures. **DSF** produces diverse forecasts that cover the diverse futures, while the other two methods appear to have collapsed to a single output.

5.5. Ablation Study

We conduct an ablation study to understand the impact of the various design choices in DSF. Specifically, we aim to understand the importance of the different parts of the DSF loss function to its empirical performance. To this end, we train four ablations of DSF-AF on nuScenes. The first two omit one of the terms in the DSF objective—i.e., one without the diversity loss (**Ours w.o. Diversity**), and one without the likelihood loss (**Ours w.o. Likelihood**). The latter two modify the DSF objectives: one replaces the NLL loss (Equation 4) with DLoW’s Reconstruction+KL losses² (**Ours w. Rec**), and one replaces the minimum in the diversity loss (Equation 5) with the mean (**Ours w. meanDiv**). All four of these models are trained using the same procedure as DSF. As shown in Table 4, the first two ablations significantly deteriorate performance. As expected, **Ours w.o. Diversity** records close to zero diversity, and **Ours w.o. Likelihood** achieves high diversity but at the cost of poor accuracy. Note that **Ours w.o. Diversity** also performs poorly in terms of accuracy; this result shows that diversity is necessary to achieve good accuracy due to the stochastic nature of future trajectories. In summary, both terms in the DSF objective are integral to its success, and taking away either completely erases its benefits.

Next, we find that **Ours w. Rec** also reduces performance. This result demonstrates that leveraging the flow model’s exact likelihood computation (i.e., having DSF directly optimize for likelihood) leads to better accuracy.

²See Appendix E for details.

Finally, **Ours w. meanDiv** significantly reduces overall performance—the prediction error increases two-fold while the diversity metrics collapse. This result demonstrates the importance of using the more robust minimum diversity metric compared to the mean diversity in the objective. In particular, the mean diversity does not penalize the degenerate case where most of the forecasts collapse to one trajectory, but one outlier forecast is very distant from the others.

Together, these ablations all validate the key design choices in DSF. We include additional ablation studies assessing DSF’s sensitivity to the quality of the underlying model as well as its training stability in Appendix E.8.

Finally, we have set the number of modes K based on predefined metrics for each dataset. However, this choice may not always be easy to make, and Appendix E.8 discusses failures due to mismatched K .

6. Conclusion

We have proposed Diversity Sampling for Flow (DSF), a learned sampling technique for pre-trained normalizing flow-based trajectory forecasting models. DSF learns a sampling distribution that induces diverse and plausible trajectory predictions. It is simple to implement, compatible with arbitrary pretrained flow-based models, and can even be trained on unlabeled data, allowing it to adapt to novel test instances on the fly. Through extensive experiments across benchmark vehicle and pedestrian detection datasets, we demonstrate that DSF consistently achieves state-of-art stochastic trajectory prediction performance.

References

- [1] Shubhankar Agarwal, Harshit Sikchi, Cole Gulino, and Eric Wilkinson. Imitative planning using conditional normalizing flow. *arXiv preprint arXiv:2007.16162*, 2020. **1**
- [2] Alexandre Alahi, Kratharth Goel, Vignesh Ramanathan, Alexandre Robicquet, Li Fei-Fei, and Silvio Savarese. Social lstm: Human trajectory prediction in crowded spaces. In *Proceedings of the IEEE conference on computer vision and pattern recognition*, pages 961–971, 2016. **5, 7**
- [3] George Awad, Asad Butt, Keith Curtis, Yooyoung Lee, Jonathan Fiscus, Afzad Godil, David Joy, Andrew Delgado, Alan Smeaton, Yvette Graham, et al. Trecvid 2018: Benchmarking video activity detection, video captioning and matching, video storytelling linking and video search. 2018. **5**
- [4] Dhruv Batra, Payman Yadollahpour, Abner Guzman-Rivera, and Gregory Shakhnarovich. Diverse m-best solutions in markov random fields. In *European Conference on Computer Vision*, pages 1–16. Springer, 2012. **2**
- [5] Holger Caesar, Varun Bankiti, Alex H Lang, Sourabh Vora, Venice Erin Liong, Qiang Xu, Anush Krishnan, Yu Pan, Giancarlo Baldan, and Oscar Beijbom. nuscnets: A multi-modal dataset for autonomous driving. In *Proceedings of the IEEE/CVF Conference on Computer Vision and Pattern Recognition*, pages 11621–11631, 2020. **1, 2, 4, 12**
- [6] Yuning Chai, Benjamin Sapp, Mayank Bansal, and Dragomir Anguelov. Multipath: Multiple probabilistic anchor trajectory hypotheses for behavior prediction. *arXiv preprint arXiv:1910.05449*, 2019. **1, 2, 5, 6**
- [7] Ming-Fang Chang, John Lambert, Patsorn Sangkloy, Jagjeet Singh, Slawomir Bak, Andrew Hartnett, De Wang, Peter Carr, Simon Lucey, Deva Ramanan, et al. Argoverse: 3d tracking and forecasting with rich maps. In *Proceedings of the IEEE Conference on Computer Vision and Pattern Recognition*, pages 8748–8757, 2019. **1**
- [8] Junyoung Chung, Caglar Gulcehre, KyungHyun Cho, and Yoshua Bengio. Empirical evaluation of gated recurrent neural networks on sequence modeling. *arXiv preprint arXiv:1412.3555*, 2014. **12**
- [9] Henggang Cui, Vladan Radosavljevic, Fang-Chieh Chou, Tsung-Han Lin, Thi Nguyen, Tzu-Kuo Huang, Jeff Schneider, and Nemanja Djuric. Multimodal trajectory predictions for autonomous driving using deep convolutional networks. In *2019 International Conference on Robotics and Automation (ICRA)*, pages 2090–2096. IEEE, 2019. **2, 4, 6**
- [10] Nicola De Cao, Wilker Aziz, and Ivan Titov. Block neural autoregressive flow. In *Uncertainty in Artificial Intelligence*, pages 1263–1273. PMLR, 2020. **2**
- [11] Nachiket Deo and Mohan M Trivedi. Convolutional social pooling for vehicle trajectory prediction. In *Proceedings of the IEEE Conference on Computer Vision and Pattern Recognition Workshops*, pages 1468–1476, 2018. **2**
- [12] Alexey Dosovitskiy, German Ros, Felipe Codevilla, Antonio Lopez, and Vladlen Koltun. Carla: An open urban driving simulator. *arXiv preprint arXiv:1711.03938*, 2017. **5**
- [13] Conor Durkan, Artur Bekasov, Iain Murray, and George Papamakarios. Neural spline flows. In *Advances in Neural Information Processing Systems*, pages 7511–7522, 2019. **2**
- [14] Mohamed Elfeki, Camille Couprie, Morgane Riviere, and Mohamed Elhoseiny. Gdpp: Learning diverse generations using determinantal point processes. In *International Conference on Machine Learning*, pages 1774–1783. PMLR, 2019. **2**
- [15] Angelos Filos, Panagiotis Tigas, Rowan McAllister, Nicholas Rhinehart, Sergey Levine, and Yariv Gal. Can autonomous vehicles identify, recover from, and adapt to distribution shifts? *arXiv preprint arXiv:2006.14911*, 2020. **2, 4, 11, 12**
- [16] Hao Fu, Chunyuan Li, Xiaodong Liu, Jianfeng Gao, Asli Celikyilmaz, and Lawrence Carin. Cyclical annealing schedule: A simple approach to mitigating kl vanishing. *arXiv preprint arXiv:1903.10145*, 2019. **2**
- [17] Boqing Gong, Wei-Lun Chao, Kristen Grauman, and Fei Sha. Diverse sequential subset selection for supervised video summarization. In *Advances in neural information processing systems*, pages 2069–2077, 2014. **2**
- [18] Agrim Gupta, Justin Johnson, Li Fei-Fei, Silvio Savarese, and Alexandre Alahi. Social gan: Socially acceptable trajectories with generative adversarial networks. In *Proceedings of the IEEE Conference on Computer Vision and Pattern Recognition*, pages 2255–2264, 2018. **1, 5, 7**
- [19] Junxian He, Daniel Spokoyny, Graham Neubig, and Taylor Berg-Kirkpatrick. Lagging inference networks and posterior collapse in variational autoencoders. *arXiv preprint arXiv:1901.05534*, 2019. **2**
- [20] Irina Higgins, Loic Matthey, Arka Pal, Christopher Burgess, Xavier Glorot, Matthew Botvinick, Shakir Mohamed, and Alexander Lerchner. beta-vae: Learning basic visual concepts with a constrained variational framework. 2016. **2**
- [21] Sepp Hochreiter and Jürgen Schmidhuber. Long short-term memory. *Neural computation*, 9(8):1735–1780, 1997. **15**
- [22] Andrew G Howard, Menglong Zhu, Bo Chen, Dmitry Kalenichenko, Weijun Wang, Tobias Weyand, Marco Andreetto, and Hartwig Adam. Mobilenets: Efficient convolutional neural networks for mobile vision applications. *arXiv preprint arXiv:1704.04861*, 2017. **12**
- [23] Chin-Wei Huang, David Krueger, Alexandre Lacoste, and Aaron Courville. Neural autoregressive flows. *arXiv preprint arXiv:1804.00779*, 2018. **2**
- [24] Boris Ivanovic and Marco Pavone. The trajectron: Probabilistic multi-agent trajectory modeling with dynamic spatiotemporal graphs. In *Proceedings of the IEEE International Conference on Computer Vision*, pages 2375–2384, 2019. **1, 2**
- [25] Thorsten Joachims. Transductive learning via spectral graph partitioning. In *Proceedings of the 20th International Conference on Machine Learning (ICML-03)*, pages 290–297, 2003. **4**
- [26] Diederik P Kingma and Jimmy Ba. Adam: A method for stochastic optimization. *arXiv preprint arXiv:1412.6980*, 2014. **13**
- [27] Steven M LaValle. *Planning algorithms*. Cambridge university press, 2006. **11**

- [28] Namhoon Lee, Wongun Choi, Paul Vernaza, Christopher B Choy, Philip HS Torr, and Manmohan Chandraker. Desire: Distant future prediction in dynamic scenes with interacting agents. In *Proceedings of the IEEE Conference on Computer Vision and Pattern Recognition*, pages 336–345, 2017. 1, 2
- [29] Junwei Liang, Lu Jiang, Kevin Murphy, Ting Yu, and Alexander Hauptmann. The garden of forking paths: Towards multi-future trajectory prediction. In *Proceedings of the IEEE/CVF Conference on Computer Vision and Pattern Recognition*, pages 10508–10518, 2020. 1, 2, 4, 5, 6, 7, 14
- [30] Junwei Liang, Lu Jiang, Juan Carlos Niebles, Alexander G Hauptmann, and Li Fei-Fei. Peeking into the future: Predicting future person activities and locations in videos. In *Proceedings of the IEEE Conference on Computer Vision and Pattern Recognition*, pages 5725–5734, 2019. 5, 7
- [31] Takeru Miyato, Toshiki Kataoka, Masanori Koyama, and Yuichi Yoshida. Spectral normalization for generative adversarial networks. *arXiv preprint arXiv:1802.05957*, 2018. 2
- [32] Sangmin Oh, Anthony Hoogs, Amitha Perera, Naresh Cuntoor, Chia-Chih Chen, Jong Taek Lee, Saurajit Mukherjee, JK Aggarwal, Hyungtae Lee, Larry Davis, et al. A large-scale benchmark dataset for event recognition in surveillance video. In *CVPR 2011*, pages 3153–3160. IEEE, 2011. 5
- [33] George Papamakarios, Eric Nalisnick, Danilo Jimenez Rezende, Shakir Mohamed, and Balaji Lakshminarayanan. Normalizing flows for probabilistic modeling and inference. *arXiv preprint arXiv:1912.02762*, 2019. 1, 2, 11
- [34] Seong Hyeon Park, Gyubok Lee, Manoj Bhat, Jimin Seo, Minseok Kang, Jonathan Francis, Ashwin R Jadhav, Paul Pu Liang, and Louis-Philippe Morency. Diverse and admissible trajectory forecasting through multimodal context understanding. *arXiv preprint arXiv:2003.03212*, 2020. 1, 2, 5, 7, 15
- [35] Tung Phan-Minh, Elena Corina Grigore, Freddy A Boulton, Oscar Beijbom, and Eric M Wolff. Covernet: Multimodal behavior prediction using trajectory sets. In *Proceedings of the IEEE/CVF Conference on Computer Vision and Pattern Recognition*, pages 14074–14083, 2020. 1, 2, 4, 6
- [36] Danilo Jimenez Rezende and Shakir Mohamed. Variational inference with normalizing flows. *arXiv preprint arXiv:1505.05770*, 2015. 2
- [37] Nicholas Rhinehart, Kris M Kitani, and Paul Vernaza. R2p2: A reparameterized pushforward policy for diverse, precise generative path forecasting. In *Proceedings of the European Conference on Computer Vision (ECCV)*, pages 772–788, 2018. 1, 2
- [38] Nicholas Rhinehart, Rowan McAllister, Kris Kitani, and Sergey Levine. Precog: Prediction conditioned on goals in visual multi-agent settings. In *Proceedings of the IEEE International Conference on Computer Vision*, pages 2821–2830, 2019. 1, 2, 12
- [39] Nicholas Rhinehart, Rowan McAllister, and Sergey Levine. Deep imitative models for flexible inference, planning, and control. *arXiv preprint arXiv:1810.06544*, 2018. 1, 2, 4, 11
- [40] Tim Salzmann, Boris Ivanovic, Punarjay Chakravarty, and Marco Pavone. Trajectron++: Multi-agent generative trajectory forecasting with heterogeneous data for control. *arXiv preprint arXiv:2001.03093*, 2020. 1, 2
- [41] Kihyuk Sohn, Honglak Lee, and Xinchen Yan. Learning structured output representation using deep conditional generative models. In *Advances in neural information processing systems*, pages 3483–3491, 2015. 3, 4
- [42] Akash Srivastava, Lazar Valkov, Chris Russell, Michael U Gutmann, and Charles Sutton. Veegan: Reducing mode collapse in gans using implicit variational learning. In *Advances in Neural Information Processing Systems*, pages 3308–3318, 2017. 2
- [43] Charlie Tang and Russ R Salakhutdinov. Multiple futures prediction. In *Advances in Neural Information Processing Systems*, pages 15424–15434, 2019. 1, 2, 5
- [44] Vladimir Vapnik and Vlamimir Vapnik. Statistical learning theory wiley. *New York*, 1:624, 1998. 2, 4
- [45] Ashish Vaswani, Noam Shazeer, Niki Parmar, Jakob Uszkoreit, Llion Jones, Aidan N Gomez, Łukasz Kaiser, and Illia Polosukhin. Attention is all you need. In *Advances in neural information processing systems*, pages 5998–6008, 2017. 5, 15
- [46] Ye Yuan and Kris Kitani. Diverse trajectory forecasting with determinantal point processes. *arXiv preprint arXiv:1907.04967*, 2019. 2, 5
- [47] Ye Yuan and Kris Kitani. Dlow: Diversifying latent flows for diverse human motion prediction. *arXiv preprint arXiv:2003.08386*, 2020. 2, 4, 5, 6, 7, 12

A. Normalizing Flow Models for Trajectory Forecasting

In this section, we review some preliminaries on normalizing flow based trajectory forecasting models. We refer readers to [33] for a comprehensive review of normalizing flows.

Normalizing flows learn a bijective mapping between a simple base distribution (e.g. Gaussian) and complex target data distribution through a series of learnable invertible functions. In this work, we denote the flow model as f_θ , where θ represents its learnable parameters. The base distribution is a multivariate Gaussian $\mathbf{Z} \sim \mathcal{N}(\mathbf{0}, \mathbf{I}) \in \mathbb{R}^{T \times 2}$, which factorizes across timesteps and (x, y) coordinates. Then, the bijective relationship between \mathbf{Z} and \mathbf{S} is captured by the following forward and inverse computations of f_θ :

$$\mathbf{S} = f_\theta(\mathbf{Z}; \mathbf{o}) \sim p_\theta(\mathbf{S} | \mathbf{o}), \quad \mathbf{Z} = f_\theta^{-1}(\mathbf{S}; \mathbf{o}) \sim P_Z \quad (6)$$

We further impose the structural dependency between \mathbf{S} and \mathbf{Z} to be an invertible autoregressive function, τ_θ , between the stepwise relative *offset* of the trajectory and the corresponding \mathbf{z} sample [39, 15]:

$$\mathbf{s}_t - \mathbf{s}_{t-1} = \tau_\theta(\mathbf{z}_t; \mathbf{z}_{<t})$$

The flow model can be trained using maximum likelihood. Because τ_θ is autoregressive (\mathbf{z}_t does not depend on any \mathbf{z}_k where $k > t$), its Jacobian is a lower-triangular matrix, which admits a simple log-absolute-determinant form [33]. The negative log-likelihood (NLL) objective is

$$\begin{aligned} & -\log p_\theta(\mathbf{S}; \mathbf{o}) \\ &= -\log \left(p(\mathbf{Z}) \left| \det \frac{d\mathbf{f}_\theta}{d\mathbf{Z}} \Big|_{\mathbf{z}=f_\theta^{-1}(\mathbf{S}; \mathbf{o})} \right|^{-1} \right) \\ &= - \left(\sum_{t=1}^T \sum_{d=1}^D \log p(\mathbf{z}_{t,d}) - \sum_{t=1}^T \sum_{d=1}^D \log \left| \frac{\partial \tau_\theta}{\partial \mathbf{z}_{t,d}} \right| \right) \end{aligned} \quad (7)$$

Once the model is trained, both sampling and *exact* inference are simple. To draw one trajectory sample \mathbf{S} , we sample $\mathbf{Z} \sim P_Z$ and compute $\mathbf{S} = f_\theta(\mathbf{Z}; \mathbf{o})$. Additionally, the exact likelihood of *any* trajectory \mathbf{S} under the model f_θ can be computed by first inverting $\mathbf{Z} = f_\theta^{-1}(\mathbf{S}; \mathbf{o})$ and then computing its transformed log probability via the change of variable formula, as in the second line of Equation 7.

B. Toy Example Details

In the example given in Figure 1(a), we simulate a vehicle either going straight or turning right at the intersection. The vehicle obeys the Bicycle dynamics [27] and uses a MPC-based controller with intermediate waypoints to guide it to its goal. In each simulation, the vehicle starts behind the bottom entrance of the intersection with a fixed initial position perturbed by white noise, and the simulation ends

when the vehicle reaches its goal. We collect 100 simulations where the vehicle’s final goal is the top exit of the intersection) and 900 simulations where the vehicle’s final goal is the right exit of the intersection. They combine into a training dataset of 1000 trajectories. Each trajectory is of 100 simulation steps. We downsample it by a factor of 10 and use the first two steps as the history input to the flow model and the task is to forecast the next 8 steps. With the first 2 steps “burned” in, the vehicle is exactly at the bottom entrance of the intersection, creating a bi-modal dataset that proves to be difficult to model for a normalizing flow model.

After the data collection, we train an autoregressive affine flow as in Appendix E.3 using the entire dataset until the log likelihood converges; Then, we sample 100 times from the flow model using i.i.d unit Gaussian inputs to create trajectories as in Figure 1(b). We train a DSF model with $K = 2$ on top of this flow model and generate 2 samples using one Gaussian noise ϵ to generate the trajectories in Figure 1(c).

C. Transductive DSF Algorithm

Algorithm 2 Transductive DSF Training

- 1: **Input:** Flow f_θ , Context \mathbf{o}
 - 2: Initialize DSF model r_ψ
 - 3: **for** $i=1, \dots, \mathbf{do}$
 - 4: Sample $\epsilon \sim \mathcal{N}(0, \mathbf{I})$
 - 5: Compute $\mathbf{Z}_1, \dots, \mathbf{Z}_K = r_\psi(\epsilon; \mathbf{o})$
 - 6: Transform $f_\theta(\mathbf{Z}_1), \dots, f_\theta(\mathbf{Z}_K)$
 - 7: Compute losses using Equations 4 & 5
 - 8: Update ψ w.r.t gradient of Equation 3
 - 9: **end for**
 - 10: Compute $\mathbf{Z}_1, \dots, \mathbf{Z}_K = r_\psi(\epsilon; \mathbf{o})$
 - 11: **Output:** $\mathcal{S} = f_\theta(\mathbf{Z}_1), \dots, f_\theta(\mathbf{Z}_K)$
-

D. DLow Details

Our implementation of DLow utilizes the same architecture as DSF. The main difference is the loss functions of the two methods. The DLow objective includes three terms:

$$\text{Reconstruction Loss} : E_r(\hat{\mathbf{s}}) = \min_{k \in K} \|\hat{\mathbf{s}}_k - \mathbf{s}\|^2$$

$$\text{Diversity Loss} : E_d(\hat{\mathbf{s}}) = \frac{1}{K(K-1)} \sum_{i \neq j \in K} \exp\left(-\frac{\|\hat{\mathbf{s}}_i - \hat{\mathbf{s}}_j\|^2}{\sigma_d}\right)$$

$$\text{KL Loss} : L_{\text{KL}}(\mathbf{z}) = \sum_{k=1}^K \text{KL}(p_\psi(\mathbf{z}_k | \mathbf{o}) \| p(\mathbf{z}_k)) \quad (8)$$

and the whole objective is:

$$L_{\text{DLow}}(\psi) = \lambda_r E_r + \lambda_d E_d + \lambda_{\text{KL}} L_{\text{KL}}$$

We tune the hyperparameters of DLow and find the following setting to work the best: $\lambda_d = 0.5, \lambda_r = 1, \lambda_{KL} = 1$, and $\sigma_d = 1$.

E. NuScenes Experimental Details

E.1. Dataset Details

NuScenes [5] is a large urban autonomous driving dataset. The dataset consists of instances of vehicle trajectories coupled with their sensor readings, such as front camera images and lidar scans. The instances are further collected from 1000 distinct traffic scenes, testing forecasting models’ ability to generalize. Following the official dataset split provided by the nuScenes development kit, we use 32186 instance for training, 8560 instances for validation, and report results on the 9041 instances in the test set.

E.2. Model Inputs

Model Inputs. All models we implement (AF, CVAE based models and MTP-Lidar) accept the same set of contextual information

$$\mathbf{o} = \{\text{Lidar scans, velocity, acceleration, yaw}\}$$

of the predicting vehicle at time $t = 0$. Below we visualize an example Lidar scan and its histogram version [38] that is fed into the models.

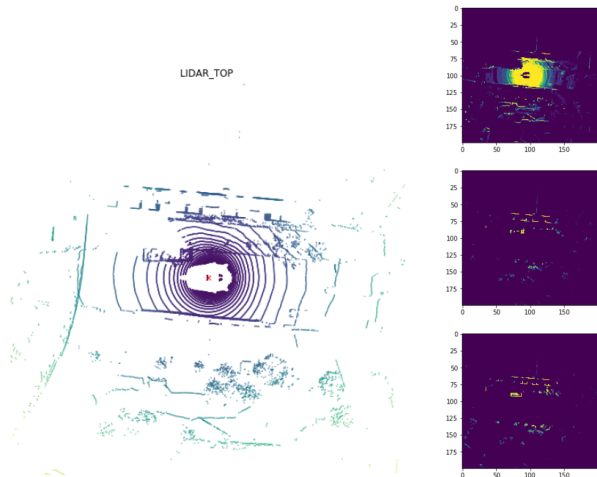


Figure 5: LiDAR inputs in nuScenes.

The Lidar scans are first processed by a pre-trained MobileNet-v128 [22] to produce visual features. These features, concatenated with the rest of the raw inputs, are passed through a neural network to produce input features for the models.

E.3. Autoregressive Affine Flow Details

Our architecture is adapted from the implementation³ provided in [15]. Here, we describe it in high level and leave the details to the architecture table provided below. AF consists of first a visual module that transforms the observation information \mathbf{o} into a feature vector \mathbf{h}_0 . Then, \mathbf{h}_0 is processed sequentially through a GRU network [8] to produce the per-step *conditioner* \mathbf{h}_t of the affine transformation: $\mathbf{h}_t = \text{GRU}(\mathbf{s}_t, \mathbf{h}_{t-1})$. Finally, we train a neural network (MLP) on top of \mathbf{h}_t to produce the modulators μ, σ of the affine transformation:

$$\begin{aligned} \mathbf{s}_t - \mathbf{s}_{t-1} &= \tau_\theta(\mathbf{z}_t; \mathbf{z}_{<t}) \\ &= \underbrace{\mu_\theta(\mathbf{s}_{1:t-1}, \phi)}_{\text{MLP}_1(\mathbf{h}_t)} + \underbrace{\sigma_\theta(\mathbf{s}_{1:t-1}, \phi)}_{\text{EXP}(\text{MLP}_2(\mathbf{h}_t))} \mathbf{z}_t \end{aligned} \quad (9)$$

Table 5: AF Architecture Overview

Attributes	Values
Visual Module	MobileNet(200 × 200 × 3, 128) Linear(128+3,64) Linear(64,64) Linear(64,64)
Autoregressive Module	GRUCell(64)
MLP Module	ReLU ◦ Linear(64,32) Linear(32, 4)
Base Distribution	$\mathcal{N}(0, \mathbf{I})$

E.4. CVAE Details

Our CVAE implementation is adapted from the implementation⁴ in [47]. It takes the same set of inputs as our AF model except the addition of a one-frame history input. The history is encoded using a GRU network of hidden size 64 to produce h_0 , which is then concatenated with the rest of the inputs. This concatenated vector is then encoded through a 2-layer fully-connected network. To encode the future, our CVAE model uses a GRU network of the same architecture as the GRU encoder for the history. Finally, the encoded input and output (i.e. future) is concatenated and passed through another 2-layer network to give the mean and the variance of the approximate posterior distribution. For the decoder, we first sample a latent vector z using the reparameterization trick. Then, z is concatenated with the encoded inputs to condition the per-step GRU roll-out of

³<https://github.com/OATML/oatomobile/blob/alpha/oatomobile/torch/networks/sequence.py>

⁴https://github.com/Khrylx/DLow/blob/master/models/motion_pred.py

the reconstructed future. The model is trained to maximize ELBO.

Table 6: CVAE Architecture Overview

Attributes	Values
History Encoder	GRU(2, 64)
Visual Module	MobileNet(200 × 200 × 3, 128)
Full Input Encoder	Linear(128+64+3, 64) Linear(64, 64) Linear(64, 64)
Full Output Encoder	GRU(2, 64)
Input Output Merger	Linear(64+64, 64) Linear(64, 32+32)
μ, σ	$\mathbb{R}^{32}, \mathbb{R}^{32}$
Decoder	GRU(2+32+64, 64) Linear(64, 64) Linear(64, 32, 2)

E.5. DSF Details

DSF r_ψ is a single multi-layer neural network with K heads, the number of modes pre-specified. To ensure stable training, we clip the diversity loss to be between $[0, 40]$ for $K = 5$ and $[0, 30]$ for $K = 10$.

Table 7: DSF Architecture and Hyperparameters Overview

Attributes	Values
DSF Architecture	Linear(Input Size, 64) Linear(64,32) Linear(32, 2 × T × K)
Learning Rate	0.001
λ_d	1
Diversity function clip value	40/30

E.6. Training Details

We train the “backbone” forecasting models AF, CVAE, MTP-Lidar for 20 epochs with learning rate 10^{-3} using Adam [26] optimizer and batch size 64. DSF-AF iterates through the full training set once, while DSF-AF-TD directly optimizes on the test set with a minibatch size of 64 and 400 adaptation iterations for every minibatch. For all DSF models, we set $\lambda_d = 1$ and do not experiment with further hyperparameter tuning. DSF training also uses Adam. For all models, we train 5 separate models using random seeds and report the average and standard deviations in our results.

E.7. Additional Results

minASD vs. meanASD. Here, we illustrate the robustness of minASD compared to meanASD. Consider the following two sets of 10 predictions. In the first set, the pairwise distance between all pairs is exactly 1. In the second set, 9 predictions are identical, but their distance to the remaining one is 100. The first set achieves identical diversity value 1 under the two metrics, whereas the second set achieves 0 minASD but $\frac{20}{9}$ meanASD. Therefore, we might incorrectly conclude that the second set is more diverse if we were to solely rely on mean metrics for diversity.

Mean diversity results. Here, we report the meanASD and meanFSD metrics for diversity. As shown, DSF still achieves the highest diversity on these metrics and provide greater diversity boost than DLow; however, the relative differences among models are much smaller. Additionally, by examining the tables from $K = 5$ to $K = 10$, we no longer find the pattern that DSF being the only model whose diversity does not deteriorate as we did in Table 2. This is because the mean metric only captures the average behavior and not the worst case behavior. Thus, our hypothesis that the min metrics are more informative than the mean metrics are supported by the following results.

Method	Samples	meanASD (\uparrow)	meanFSD (\uparrow)
MTP-Lidar-5	5	5.74 ± 0.79	13.80 ± 2.00
CVAE	5	5.38 ± 0.09	12.28 ± 0.16
DLow-CVAE	5	6.66 ± 0.21	15.43 ± 0.44
AF	5	6.21 ± 0.02	14.48 ± 0.04
DLow-AF-5	5	7.41 ± 0.29	17.90 ± 0.67
DSF-AF-5	5	7.89 ± 0.29	19.06 ± 0.58

Method	Samples	meanASD (\uparrow)	meanFSD (\uparrow)
MTP-Lidar-10	10	5.24 ± 0.30	12.71 ± 0.59
CVAE	10	5.38 ± 0.10	12.28 ± 0.18
DLow-CVAE	10	6.96 ± 0.20	16.16 ± 0.45
AF	10	6.21 ± 0.01	14.48 ± 0.04
DLow-AF-10	10	7.88 ± 0.57	19.49 ± 1.36
DSF-AF-10	10	7.90 ± 0.28	19.71 ± 0.74

Table 8: NuScenes prediction mean diversity results.

E.8. Additional Ablation Results

In this section, we provide some additional ablation studies to further understand the effectiveness of DSF. First, we aim to understand: **how sensitive is DSF to the quality of the underlying flow model?** To answer this question, we train an additional AF model with half the number of epochs as the original one (**AF⁻**), and then train DSF as before. The comparisons are shown in Table 9. With only

half the training time, AF^- performs considerably worse than AF, yet DSF is still able to provide a significant performance boost, achieving **33%** reduction in both minADE and minFDE. This reduction is greater than that of DSF applied to the stronger AF model (27%), suggesting the utility of DSF is greater for weaker pre-trained model and highlighting that its overall effectiveness is robust to the quality of the underlying flow.

Method	S	mADE ₅	↓%	mFDE ₅	↓%	minASD	↑%	minFSD	↑%
AF^-	5	3.49 ± 0.16	-	7.79 ± 0.41	-	1.99 ± 0.15	-	4.58 ± 0.46	-
DSF- AF^-	5	2.31 ± 0.19	34%	5.17 ± 0.39	34%	2.91 ± 0.05	146%	8.25 ± 0.32	180%
DSF- AF^- -TD	5	2.35 ± 0.16	33%	5.24 ± 0.33	33%	3.00 ± 0.16	151%	8.36 ± 0.14	183%
AF	5	2.86 ± 0.01	-	6.26 ± 0.05	-	1.58 ± 0.02	-	3.75 ± 0.04	-
DSF-AF	5	2.06 ± 0.09	28%	4.67 ± 0.25	25%	3.13 ± 0.18	98%	8.19 ± 0.26	118%
DSF-AF-TD	5	2.06 ± 0.02	28%	4.62 ± 0.07	26%	3.09 ± 0.07	95%	8.15 ± 0.17	117%

Table 9: DSF ablations on the pre-trained flow models.

DSF training stability. We track the state of minADE and minASD on the mini nuScenes validation set over the course of DSF training. On the mini version of the nuScenes dataset, we train a DSF-AF ($K = 5$) model, and for every training iteration, we compute the current DSF-AF model’s minADE and minASD on the mini validation set. The mini version is a much smaller dataset with only 1000 instances, making this procedure manageable. The sequence of (ASD, ADE) pairs are traced as a trajectory on a 2D plane, where the x-axis corresponds to minASD₅ and the y-axis corresponds to minADE₅.

The entire trajectory is visualized in Figure 6. We additionally visualize both minADE and minASD individually over the course of training in the middle and the right panels. In all three plots, the initial AF model’s (ASD, ADE) point is colored in red, and the final DSF-AF’s (ASD, ADE) point is colored in blue. Focusing on the left panel, we note that the initial point at the top left corner represents the ADE/ASD of the pre-trained flow backbone, which has relatively high error and low diversity. However, DSF quickly discovers good sampling distribution and offers fast and near “monotonic” improvements along both axis. This provides evidence that the joint objective is effective and helps avoiding potential local minima in the loss landscape. The rapid improvement early on in training also explains why DSF’s transductive adaptation procedure can be effective. Finally, an early stopping mechanism may be effective given the fast convergence to the optimum (i.e. the bottom right corner); we leave it to future work to investigate the precise stopping criterion.

Mismatched K. Here, we perform a controlled experiment analyzing DSF outputs when the number of samples K it learns to output mismatches the number of modes in the underlying distribution. To do this, we return to our toy

intersection environment as in Figure 1(a). Instead of training a DSF with $K = 2$ as done in Figure 1(c), we train one with $K = 5$. This DSF’s set of 5 samples are shown in Figure 7. Among the 5 trajectories, the two modes are still captured. Importantly, the major mode (turning right) is captured twice. However, the remaining two trajectories represent the average of the two modes and correspond to potentially unrealistic behaviors. Note that this set of five trajectories would achieve very low minADE errors in both single and multiple-future evaluations, since at least one trajectory in the predictions is close to both modes. However, for planning settings, this set of predictions may not be optimal. Hence, choosing K carefully is important in practice, and we leave it to future work for further investigations.

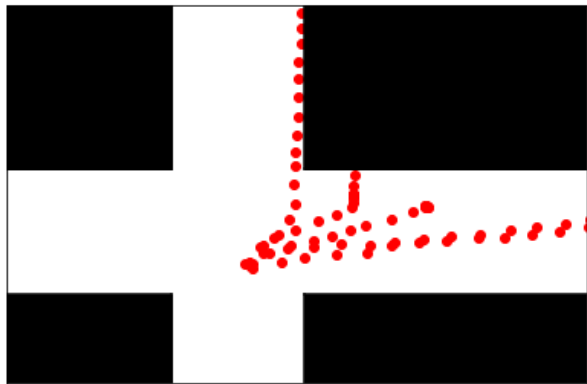


Figure 7: DSF outputs for $K = 5$.

E.9. Additional Visualizations

In this section, we provide additional visualizations of DSF, AF, and MTP-Lidar outputs (Figure 8).

F. Forking Paths Experimental Details

F.1. Dataset Details

Here, we briefly describe the Forking Paths evaluation dataset [29]. FP semi-automatically reconstruct static scenes and their dynamic elements (e.g. pedestrians) from real-world videos in ActEV/VIRAT and ETH/UCY in the CARLA simulator. To do so, it converts the ground truth trajectory annotations from the real-world videos to coordinates in the simulator using the provided homography matrices of the datasets. Then, 127 “controlled agents” (CA) are selected from the 7 reconstructed scenes. For each CA, there are on average 5.9 human annotators to control the pedestrian to the pre-defined destinations in a “natural” way that mimics real pedestrian behaviors. The scenes are also rendered to the annotators in different camera angles ranging from ‘Top-Down’ to ‘45-Degree’. The annotation can last up to 10.4 seconds, which is far longer than the 4.8 sec-



Figure 6: **Left:** DSF (ASD, ADE) plot on nuScenes mini. DSF offers stable and fast improvements to flow outputs in both accuracy and diversity during its training. **Middle:** DSF ADE over the course of training. **Right:** DSF minASD over the course of training.

onds prediction window in the original datasets, making the forecasting problem considerably harder. In total, there are 750 trajectories after data cleaning.

F.2. CAM-NF Model Details

CAM-NF [34] consists of an encoder-decoder architecture. The encoder includes a cross-agent interaction module using self-attention [45]. The decoder is an autoregressive affine flow similar to the one used for nuScenes. Here, we briefly describe the architectures and refer interested readers to the original work.

The encoder first uses an LSTM of hidden dimension 512 [21] to extract a history embedding for every agent up to the most recent timestep $t = 0$:

$$h_t^a = \text{LSTM}(\mathbf{s}_{t-1}^a, h_{t-1}^a) \quad t = T_{\text{hist}} - 1, \dots, 0$$

Then, the history embedding of all agents h_t^0, \dots, h_t^A are aggregated to compute a corresponding cross-agent attention embedding using self-attention. This embedding is then combined with the history embedding to form the inputs to the normalizing flow decoder:

$$\tilde{h}^a = h_0^a + \text{SELF-ATTENTION}(Q^a, \mathbf{K}, \mathbf{V})$$

where (Q^a, K^a, V^a) is the query-key-value triple for each agent, and the bold versions are their all-agent aggregated counterparts. Note that \tilde{h}^a is passed through a linear layer of hidden dimension 256 before passed to the decoder.

The decoder is similar to the autoregressive affine flow used for nuScenes with a few minor changes. First, $\sigma_\theta \in \mathbb{R}^{2 \times 2}$ to model correlation between the two dimensions (i.e. x, y) of the states. Second, a velocity smoothing term $\alpha(\mathbf{s}_{t-1} - \mathbf{s}_{t-2})$ is added to the step-wise update. That is,

$$\begin{aligned} \mathbf{s}_t - \mathbf{s}_{t-1} &= \tau_\theta(\mathbf{z}_t; \mathbf{z}_{<t}) \\ &= \alpha(\mathbf{s}_{t-1} - \mathbf{s}_{t-2}) + \underbrace{\mu_\theta(\mathbf{s}_{1:t-1}, \phi)}_{\text{MLP}_1(\mathbf{h}_t)} + \underbrace{\sigma_\theta(\mathbf{s}_{1:t-1}, \phi)}_{\text{EXP}(\text{MLP}_2(\mathbf{h}_t))} \mathbf{z}_t \end{aligned} \quad (10)$$

We set $\alpha = 0.5$ as in the original work. Our implementation is adapted from the original implementation⁵.

F.3. DSF & DLow Details

Since trajectories in FP have different lengths, we set $T = 25$ in the DSF architecture to ensure that a bijective mapping between $\mathbf{Z} \in \mathbb{R}^{T \times D}$ exists for all samples in FP. This also means that during training, we optimize DSF for up to 25 steps. We also slightly increase the size of DSF neural network and set the maximum diversity loss to be 80, which we find to work well empirically. As before, DLow uses the same architecture. The whole architecture is as follows:

Table 10: DSF Architecture and Hyperparameters Overview

Attributes	Values
DSF Architecture	Linear(Input Size, 128) Linear(128,64) Linear(64, $2 \times 25 \times K$)
Learning Rate	0.001
λ_d	10
Diversity function clip value	80

F.4. Training Details

We train CAM-NF for 200 epochs with learning rate 10^{-3} using Adam optimizer and batch size 64. We train DSF, DSF-TD, and DLow models using mode hyperparameter $K = 20$. DSF and DLow iterate through the full training set once, while DSF-AF-TD directly optimizes on the test set with a minibatch size of 64 and 200 adaptation iterations for every minibatch. For all DSF models, through a hyperparameter search, we set $\lambda_d = 10$. For all models, we train 5 separate models using random seeds and report the average and standard deviations.

⁵<https://github.com/kami93/CMU-DATF>

F.5. Additional Visualizations

In this section, we provide some additional visualizations of DSF, CAM-NF, and Multiverse outputs (Figure 9).

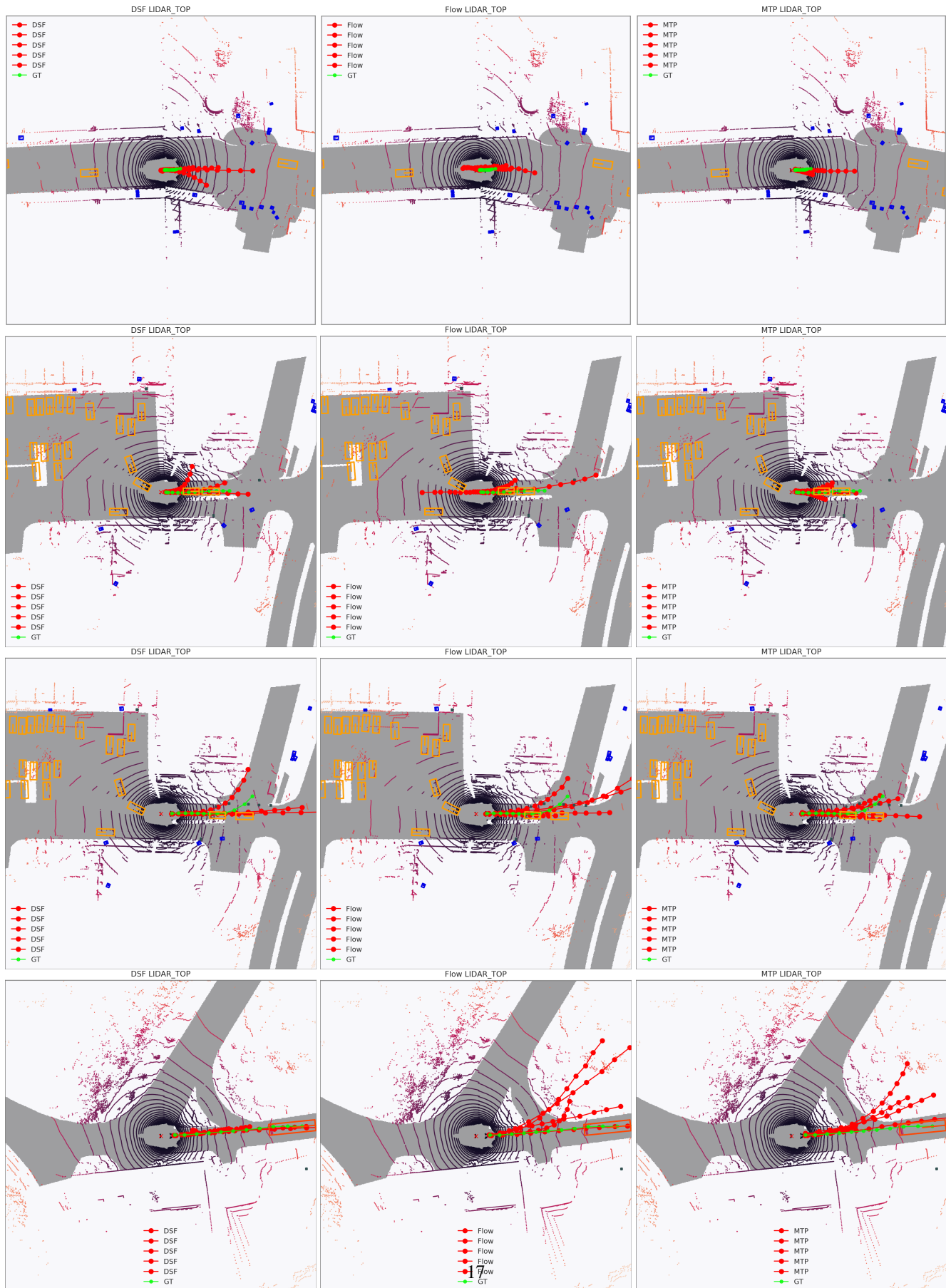


Figure 8: Additional model visualizations. The models from left to right: **DSF**, **AF**, and **MTP-Lidar**.

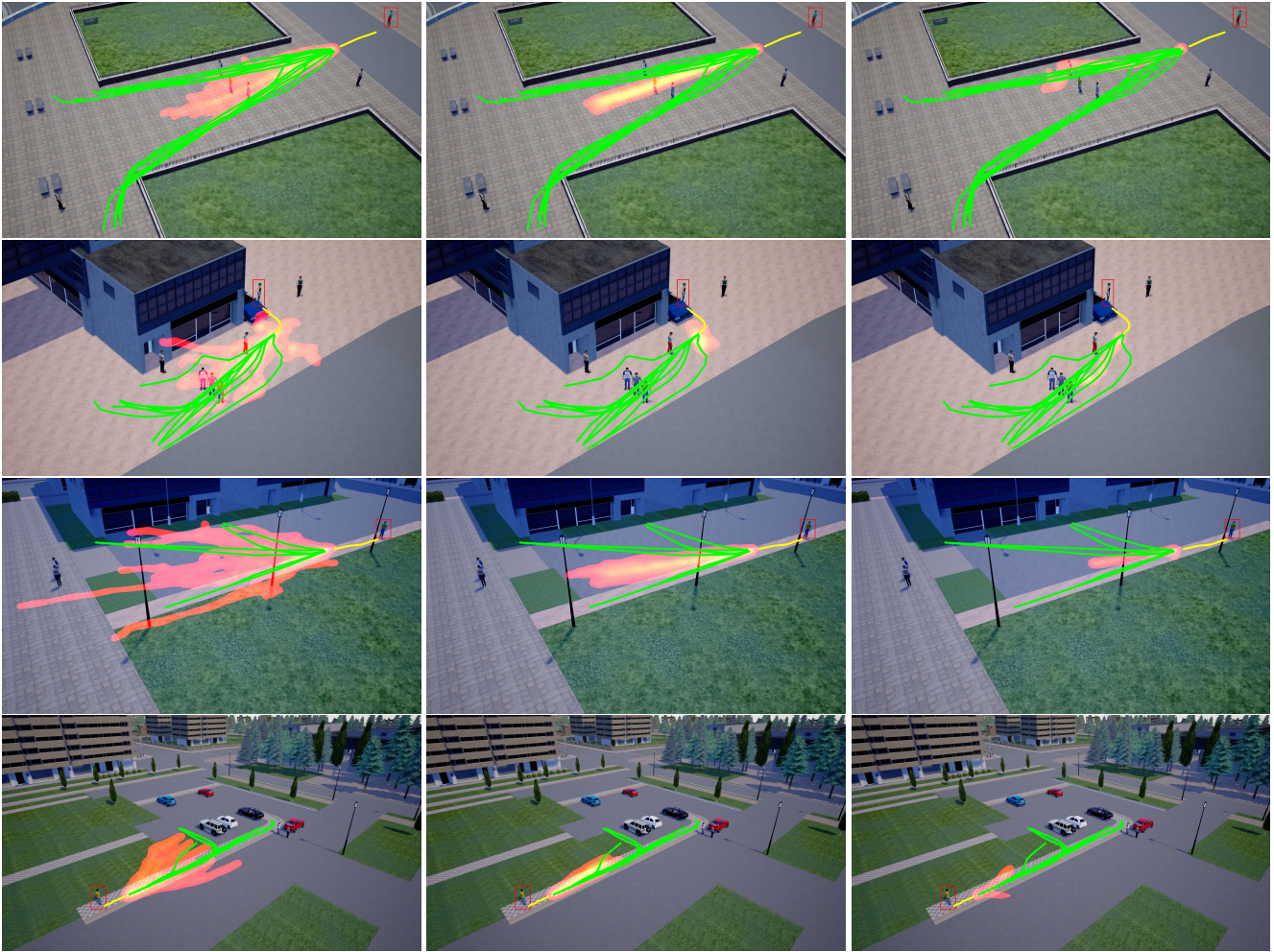


Figure 9: Additional model visualizations. The models from left to right: **DSF**, **CAM-NE**, and **Multiverse**.